JGR Oceans

RESEARCH ARTICLE
10.1029/2021JC018222

Wind Fetch and Direction Effects on Langmuir Turbulence in a Coastal Ocean

Xingchi Wang[1], Tobias Kukulka[1], and Albert J. Plueddemann[2]

[1]University of Delaware, Newark, DE, USA, [2]Woods Hole Oceanographic Institution, Woods Hole, MA, USA

Key Points:

- Oblique offshore winds drive strong wind and wave misalignment due to longer along-shore but limited offshore wind fetches
- Coherent Langmuir turbulence characteristics are predominantly observed under conditions of developed and wind-aligned waves
- Large eddy simulations agree well with observed Langmuir turbulence characteristics in a fetch-limited coastal ocean

Correspondence to:
X. Wang,
wangxch@udel.edu

Citation:
Wang, X., Kukulka, T., & Plueddemann, A. J. (2022). Wind fetch and direction effects on Langmuir turbulence in a coastal ocean. *Journal of Geophysical Research: Oceans*, *127*, e2021JC018222. https://doi.org/10.1029/2021JC018222

Received 8 NOV 2021
Accepted 18 APR 2022

Abstract Mixing processes in the upper ocean play a key role in transferring heat, momentum, and matter in the ocean. These mixing processes are significantly enhanced by wave-driven Langmuir turbulence (LT). Based on a paired analysis of observations and simulations, this study investigates wind fetch and direction effects on LT at a coastal site south of the island Martha's Vineyard (MA, USA). Our results demonstrate that LT is strongly influenced by wind fetch and direction in coastal oceans, both of which contribute to controlling turbulent coastal transport processes. For northerly offshore winds, land limits the wind fetch and wave development, whereas southerly winds are associated with practically infinite fetch. Observed and simulated two-dimensional wave height spectra reveal persistent southerly swell and substantially more developed wind-driven waves from the south. For oblique offshore winds, waves develop more strongly in the alongshore direction with less limited fetch, resulting in significant wind and wave misalignments. Observations of coherent near-surface crosswind velocities indicate that LT is only present for sufficiently developed waves. The fetch-limited northerly winds inhibit wave developments and the formation of LT. In addition to limited fetch, strong wind–wave misalignments prevent LT development. Although energetic and persistent, swell waves do not substantially influence LT activity during the observation period because these relatively long swell waves are associated with small Stokes drift shear. These observational results agree well with turbulence-resolving large eddy simulations (LESs) based on the wave-averaged Navier–Stokes equation, validating the LES approach to coastal LT in the complex wind and wave conditions.

Plain Language Summary The ocean surface boundary layer is part of the upper ocean and couples the ocean and atmosphere. Wind and waves inject energy and momentum into this layer that transport and mix ocean properties such as velocity, temperature, salinity, and suspended and dissolved matter. Ocean observation at a coastal site shows that the wind directions and the distances from shore available for wave development can lead to misalignments of wind and waves. Both observation and numerical model results demonstrate that the misalignments of wind and waves further impact the mixing processes driven by wind and waves. The aligned wind and waves result in stronger ocean mixing than the misaligned ones. In addition, the agreement of observation and numerical results validates the numerical model for the coastal ocean mixing under complex wind and wave conditions. Our results help better understand the transport and mixing processes in coastal oceans.

1. Introduction

Langmuir turbulence (LT) is an important turbulent process in the ocean surface boundary layer (OSBL), significantly affecting the transports of heat, salt, momentum, and suspended and dissolved matter. LT is formed by the Craik–Leibovich (CL) vortex force (Craik & Leibovich, 1976) that results in counterrotating vortices approximately aligned with the wind, so called Langmuir circulations. Those coherent vortex pairs of LT generate strong surface convergent regions and downwelling jets, enhancing the OSBL mixing (Grant & Belcher, 2009; Kukulka et al., 2009; McWilliams et al., 1997). Turbulence-resolving large eddy simulation (LES) models based on the filtered CL equation (McWilliams et al., 1997; Skyllingstad & Denbo, 1995) succeed in reproducing important LT characteristics that have been observed earlier, such as nearly wind-aligned coherent surface convergent regions (D'Asaro, 2014; Farmer & Li, 1995; Plueddemann et al., 1996; Smith, 1992; Thorpe, 2004) and enhanced vertical mixing due to counterrotating roll vortices (Gargett et al., 2004; Weller et al., 1985). The goal of this research is to improve understanding of LT processes in coastal oceans and investigate the effects of wind fetch and direction on LT activity. Additionally, this study is aimed at providing rare observational evidence for wind–wave misalignment effects on LT.

Traditionally, LT studies have focused on open ocean environments, although more recent work suggests that LT is also critical in coastal oceans, playing an important role in coastal turbulent transport processes (Gargett et al., 2004; Sullivan & McWilliams, 2010; Thorpe, 2004). Observations indicate that full-depth LT can form in depth-limited coastal oceans (Gargett et al., 2004) and couples the mixing processes at both surface and bottom boundary layers (Gargett & Wells, 2007). For aligned wind and waves, idealized coastal LES results are consistent with field observations (Kukulka et al., 2012; Tejada-Martínez & Grosch, 2007). These LES studies indicate that LT is associated with organized roll vortices that are characterized by strong crosswind velocity convergences near the surface and enhanced downwind velocities in downwelling regions. Moreover, full-depth LT redistributes turbulent kinetic energy (TKE), disrupting the logarithmic layer, and transports momentum away from the boundary (Deng et al., 2019; Kukulka et al., 2012; Tejada-Martínez et al., 2012). However, wave fields at a coastal site are usually complex with swell waves and frequently misaligned wind and waves (Churchill et al., 2006; Kukulka et al., 2017). This study considers how these conditions impact LT development.

This study uses observations from the Coupled Boundary Layer and Air–Sea Transfer Experiment in Low Winds (CBLAST-low) to examine coastal LT under complex wind and wave conditions. The CBLAST-low experiment was conducted on the west Atlantic continental shelf near Martha's Vineyard and provided comprehensive measurements for the atmosphere and ocean (Edson et al., 2007; Gerbi et al., 2009). This data set has been analyzed extensively to investigate boundary layer turbulence in a coastal ocean. Observed TKE dynamics suggests that TKE transport is critical in the wave-driven OSBL (Gerbi et al., 2009). These observational results are consistent with LES results that demonstrates enhanced TKE input and transport by breaking waves and LT (Li et al., 2013). Coherent LT structures in near-surface velocity have also been observed, which may be distorted by tidal currents (Kukulka et al., 2011, 2012). As a first step, these previous studies did not focus on the effects of wind–wave misalignment and complex fetch on LT dynamics.

Recent LES studies shows that LT weakens as the misalignment of wind and waves increases (Van Roekel et al., 2012; X. Wang & Kukulka, 2021). The direction of LT horizontally elongated turbulent structure, defined as the direction of Langmuir cells, also depends on the misalignments of wind and waves and generally aligns with the surface layer depth-averaged Lagrangian velocity shear (the sum of Stokes drift shear and Eulerian velocity shear, Van Roekel et al., 2012; D. Wang et al., 2019). For the situations of misaligned wind and waves, the crosswind Stokes drift plays a key role in generating TKE and turbulent stress, which are not well parameterized in Reynolds-averaged Navier–Stokes models (Pearson et al., 2019; D. Wang & Kukulka, 2021). X. Wang and Kukulka (2021) showed that the wind–wave misalignment induced by rapidly turning winds leads to weaker turbulence and a transition from LT to shear-driven turbulence (ST) despite the presence of strong waves.

Misalignment of wind and waves may occur in the open or coastal ocean, but coastal ocean conditions make wind–wave misalignment, as well as misaligned wind waves and swell, more likely. In the coastal ocean, short wind fetch limits the development of wind-driven waves, forming younger waves (Van Den Bremer & Breivik, 2018). The associated smaller Stokes drift shear for younger waves reduces LT throughout the OSBL compared to more developed wind-driven seas (Harcourt & D'Asaro, 2008; Kukulka & Harcourt, 2017), so that the fetch limitation can further influence LT. Comparison between lake and open ocean observations indicates that limited wind fetch significantly reduces turbulent vertical velocity variance and, thus, LT activity (D'Asaro et al., 2014). Moreover, fetch limitations control the direction of wind-driven waves; for example, measurements in Chesapeake Bay reveal common and persistent wind–wave misalignments (Fisher et al., 2017). The wind–wave misalignments significantly affect LT activity. Idealized LES results with prescribed wind and waves indicate that increased wind–wave misalignment can diminish the coherent structure of LT but have a negligible influence on the direction of Langmuir cells in the coastal oceans (Shrestha et al., 2019).

Based on a systematic analysis of coastal observations and LES results driven by realistic wind–wave forcing, this study explores wind fetch and direction effects on coastal LT. In the next section, we review our observational and numerical modeling approaches and also identify observed events with different wind and wave misalignments which are investigated in greater depth. In Section 3, we first explore how different wind directions affect fetch-limited waves and wind–wave misalignments and then demonstrate that these complex coastal wind and wave conditions strongly influence LT.

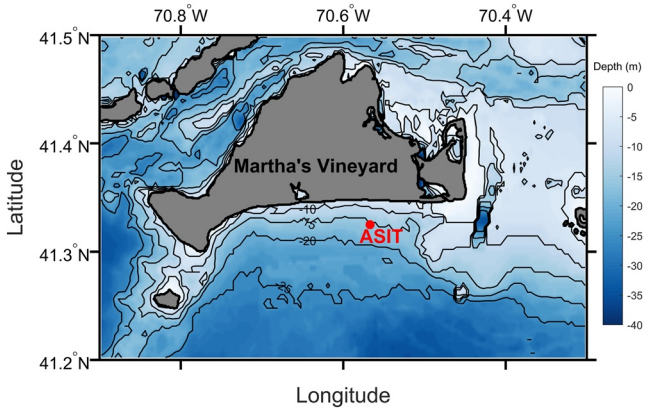

Figure 1. Map showing the location of Air–Sea Interaction Tower (ASIT). Color represents the ocean depths and contours show isobaths between 10 and 25 m.

2. Methods

2.1. Observations

2.1.1. CBLAST-Low Experiment

This study utilizes the data from the CBLAST-low, which was conducted on the west Atlantic continental shelf during 2001 and 2003 about 3 km south of Martha's Vineyard, MA, USA (Figure 1, Edson et al., 2007; Gerbi et al., 2009). For direct and simultaneous measurements on both sides of the air–sea interface, the bottom-fixed Air–Sea Interaction Tower (ASIT) was deployed during the CBLAST-low experiment with a depth of about $H = 16$ m (Figure 1). Meanwhile, two-dimensional ocean surface wave fields were also measured by a 1,200-kHZ ADCP at the seafloor node, about 1 km shoreward of the ASIT (Gerbi et al., 2009). Here, we analyze the observed air–sea fluxes of momentum and wave fields to understand the meteorological conditions for the CBLAST-low experiment (Figure 2).

In addition, we use the same CBLAST-low fan-beam ADCP data as in Gerbi et al. (2009) and Kukulka et al. (2011, 2012) to detect LT activity. This fan-beam ADCP uses traditional ADCP electronics but with a modified transducer head that generates four narrow-azimuth beams to measure the horizontal velocities of surface trapped bubbles to obtain the horizontal velocities of near-surface currents (Plueddemann et al., 2001; Smith, 1989; Zedel & Farmer, 1991). In the presence of LT, the fan-beam ADCP can detect horizontal bands due to the velocity

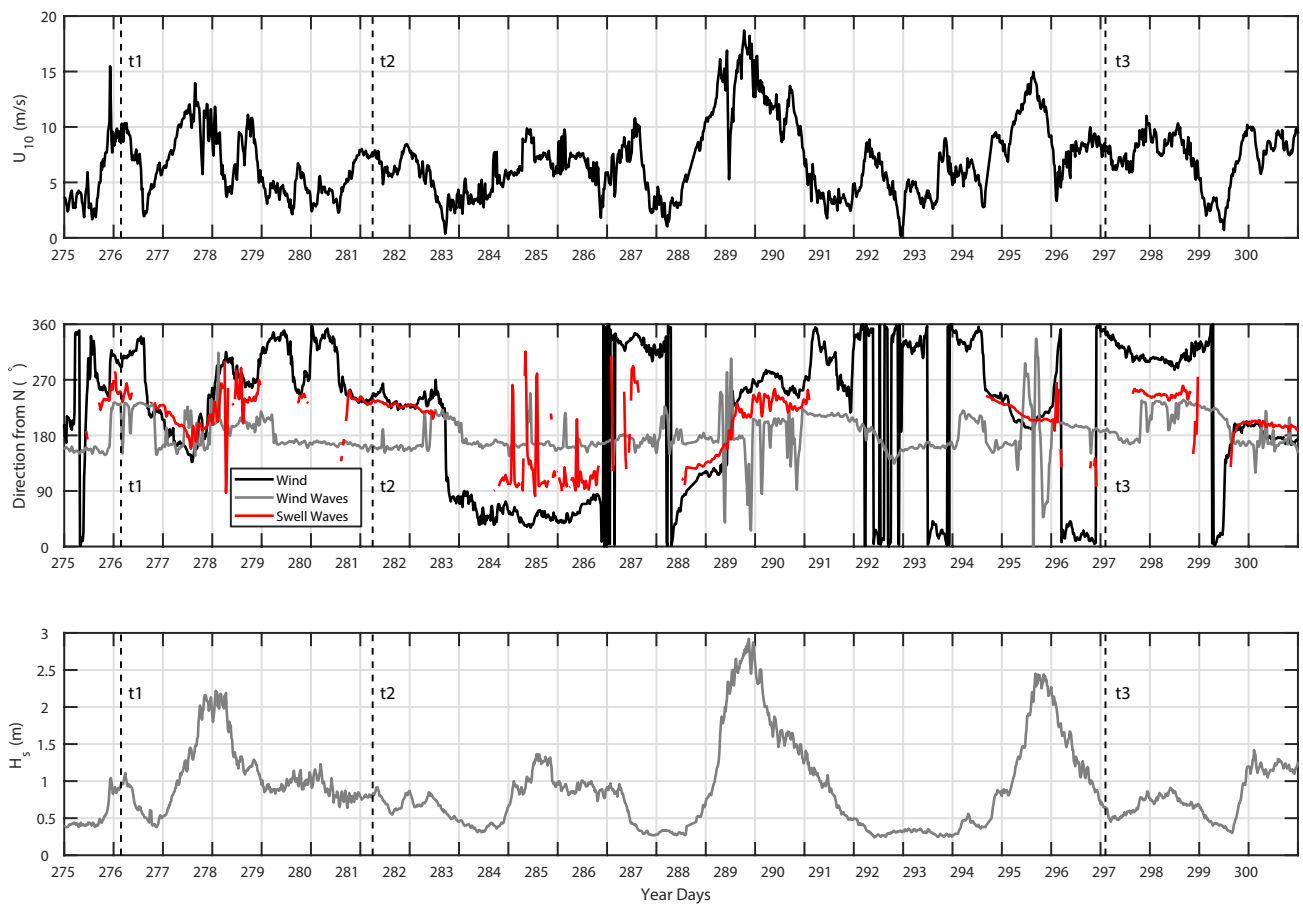

Figure 2. Wind and wave conditions during the CBLAST-low experiment. (top) Wind speed at 10 m height; (center) directions of wind (black line), wind waves (red line), and swell waves (gray line); and (bottom) significant wave height. Vertical dashed lines indicates three events (t1–t3) with relatively constant wind speeds but different wind–wave misalignments.

convergence and divergence zones formed by the coherent surface LT structures when the sonar beams intersect with the wind direction. We focus on the period from the end of September to the beginning of November in 2003 during fan-beam ADCP deployment. The wave fields are partitioned into locally generated wind-driven waves and swell waves using the analysis from Churchill et al. (2006) based on the method of Hanson and Phillips (2001). During this period, winds are variable, and wind and waves are misaligned at times (Figure 2). This study does not examine buoyancy effects due to air–sea heat fluxes because the measured density differences between near-surface and near-bottom are generally small and the Monin–Obukhov length is usually much larger than the ocean depth during most of the analysis period (Kukulka et al., 2011).

Following the methods of Kukulka et al. (2011, 2012), we use a conservative, fixed aperture of 85 m that contains several horizontally distributed "range cells," which can detect the spatial scales no longer than 85 m. The "range cells" are about 2.4 m along beam and 5 m cross beam. The ping rate of fan-beam ADCP was 1 Hz, with 56 ping ensembles recorded every minute. The same processing as in Kukulka et al. (2011, 2012) are used to extract a robust signal of near-surface velocity convergence regions from the noisy acoustic measurements. In those studies, a 40 min temporal high-pass filter is first applied on fan-beam velocity to remove tidal variability. The high-passed velocity is then detrended in time and space for each 20 min interval. A moving average with 14 m window along beam direction is also applied to obtain the velocity anomaly for LT-induced large-scale surface velocity structures. This study selects the beam most orthogonal to the winds for detecting the LT-induced strong crosswind velocity. The processed fan-beam near-surface velocity anomaly u'_f is a function of time and fan-beam range (Kukulka et al., 2011, 2012). For strong LT events, u'_f displays relatively strong and coherent near-surface crosswind velocity convergences and divergences. For weak LT events, the u'_f pattern of convergences and divergences is less organized, and the turbulence is mainly driven by shear-instabilities with a relatively disordered u'_f. Moreover, the root-mean-square of u'_f calculated over the fan-beam range and 20 min contiguous intervals is also used to quantify LT strength, denoted as VRMS. The strong crosswind surface convergence/divergence regions are often observed for VRMS $\geq$ 1.1 cm/s when wind and wave are aligned (Kukulka et al., 2011).

2.1.2. Misaligned Wind and Waves During CBLAST-Low

At the study site, wind directions are highly variable covering all quadrants (Figure 2). In contrast, waves propagate predominantly toward north, so that wind and waves are often substantially misaligned. In this study, the directions of winds and waves are defined meteorologically (direction from) unless otherwise specified.

A statistical analysis of wind–wave alignments for the whole observation period indicates three representative conditions: (a) relatively well-aligned wind and waves (onshore and oblique onshore winds) or sustained wind–wave misalignments due to (b) oblique offshore winds and (c) offshore winds. These three cases are the focus of the further investigation. We analyze three distinct events representing typical observed wind fetch and wind–wave misalignment conditions that capture the important dynamics. By contrasting all three cases and simulating their upper ocean response, we will be able to investigate the effects of wind fetch and wind–wave misalignment on LT. To minimize the influence of wind speeds, we select events with similar moderate wind speeds (wind speeds at 10 m height U_{10} is around 8 m/s) but with different wind directions. For the first, second, and third events (t1, t2, and t3 in Figure 2), the wind directions are about 325°, 240°, and 360°, respectively. For t1 and t3, wind and waves are misaligned as their winds have offshore components limited by short wind fetch, while the t2 winds blow from the ocean with a roughly infinite wind fetch, forming an aligned wind and waves (Figure 3). Because the transient wind forcing can lead to a significant variation of ocean turbulence in the mixing layer (X. Wang & Kukulka, 2021), we also require that each event has been driven by relatively constant wind and waves for over 6 hr to dismiss the effects from nonstationary forcing. Moreover, horizontal mean currents may disrupt the LT and alter Langmuir cell directions (Kukulka et al., 2011; Li et al., 2013; Shrestha et al., 2019) so that our selected events are also during times with weak crosswind currents to avoid tidal current influences.

2.2. Numerical Model Experiments

2.2.1. Spectral Wave Model

To understand the relationship between wind direction and wind–wave misalignment in the fetch-limited ocean near Martha's Vineyard, we design several idealized wave simulation experiments employing the spectral wave model Simulation Wave Nearshore (SWAN; Booij et al., 1997). The SWAN experiments mimic the geographic

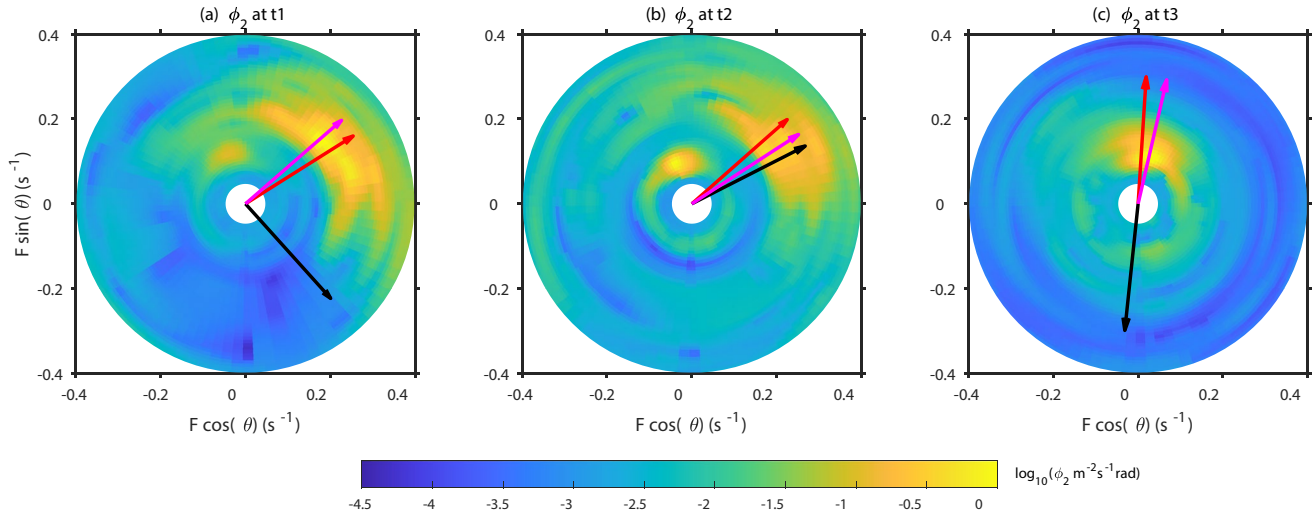

Figure 3. Observed two-dimensional wave height spectra for specific events in Figure 2, where F is the wave frequency, and θ is the wave propagation direction. Arrows represent the directions of wind (black arrow), wave (magenta arrow), and surface Stokes drift (red arrow). The wave propagation and arrow directions use Cartesian convention.

setting of the CBLAST-low site so that a land boundary is imposed to the north, and the ocean is practically unbounded to south, east, and west. The ocean depth is set to 16 m for the entire domain, consistent with the depth of CBLAST-low site. Sensitivity tests with a more realistic gradually sloped bathymetry indicate that the influence of bathymetric refraction on the development of wave spectra is not important at this site (not shown here).

The spatial domain of the wave model is set to 1D mode with a domain size of 150 km south to north with a 1 km spatial resolution and infinite fetch in the west-east direction. Note that waves are still allowed to propagate in two dimensions with this setting. This setup provides an unbounded ocean toward east and west while fetch to the south is sufficiently long, consistent with the CBLAST-low site. Tests with larger domains and higher resolutions are also performed to validate the robustness of the selected domain setting. The wave spectrum is discretized into 90 evenly spaced directions with $\Delta\theta = 4°$, and 36 logarithmically spaced frequencies F ranging from 0.0418 to 1.2 Hz with $\Delta F = 0.1F$. To focus on the fetch influence, we employ the default SWAN settings of wave physics and boundary conditions that do not include the wave reflection at the boundaries. Three wind directions are imposed in the SWAN experiments to represent the wave responses to different wind directions. Corresponding to events t1, t2, and t3 (Figure 2), the wind directions of three SWAN experiments are 325° (experiment NW), 240° (experiment SW), and 360° (experiment N), respectively. The wind speed is set constant to 8 m/s for all experiments. The wave model runs in a stationary mode to ensure stationary wave fields that focus on the effects of wind direction and wind fetch limitations.

2.2.2. Coastal LES

This study utilizes a coastal turbulence-resolving LES model, which has been applied in Kukulka et al. (2011, 2012). This coastal LES model was modified based on a laterally periodic LES model designed for open ocean (McWilliams et al., 1997). The open ocean LES model is based on the grid-filtered CL equations with governing momentum equations as follows:

$$\frac{\partial \tilde{u}_i}{\partial t} + \tilde{u}_j \frac{\partial \tilde{u}_i}{\partial x_j} = -\frac{\partial \tilde{\pi}}{\partial x_i} + \frac{\tilde{\rho}}{\rho_0} g_i + \epsilon_{ikm} u_{s,k} \tilde{\omega}_m + SGS, \tag{1}$$

where t denotes time; the Cartesian coordinates $(x_1, x_2, x_3) = (x, y, z)$ include components toward east, north, and upward, respectively; $(u_1, u_2, u_3) = (u, v, w)$ is the velocity vector; $(u_{s,1}, u_{s,2}, u_{s,3}) = (u_s, v_s, 0)$ is the Stokes drift vector; $(g_1, g_2, g_3) = (0, 0, -g)$ is the Earth's acceleration vector with $g = 9.81$ m/s^2; $\pi = p/\rho_0 + 1/2[(u_i + u_{s,i})(u_i + u_{s,i}) - u_i u_i]$ is the generalized pressure in which p is the pressure; ρ is the water density; $\omega_i = \epsilon_{ikm}(\partial/\partial x_k)u_m$ is the relative vorticity; and ϵ_{ikm} is the permutation tensor. Most coastal LT studies based on LES (e.g., Kukulka et al., 2011, 2012; Tejada-Martínez & Grosch, 2007) neglect the Coriolis force and agree well with observations. One reason is that the coastal boundary sets up barotropic pressure gradients so that the cross-shelf flow

is relatively weak and the flow resembles that of a wind stress-driven flow without Coriolis force (Lentz, 1995). Following previous studies (Kukulka et al., 2011, 2012; Shrestha et al., 2019; Tejada-Martínez & Grosch, 2007), the Earth's rotation is not considered in the LES model. The LES method decomposes variables into resolved, indicated by tilde, and subgrid-scale components denoted by SGS (Moeng, 1984). The turbulent SGS fluxes are parameterized via an SGS eddy viscosity depended on SGS TKE, which is solved by a prognostic equation. The CL vortex force $\epsilon_{ikm}u_{s,k}\omega_m$ describes the interaction between nonbreaking waves and Eulerian currents. The CL vortex force is zero for ST so that the LES model simply captures shear and buoyancy instabilities.

Unlike the open ocean LES, the coastal LES implements a solid wall bottom boundary condition based on the atmospheric approach from Sullivan et al. (1994). The bottom stress is parameterized by a drag coefficient $C_D = 0.0034$, and the roughness length of $z_0 = 0.75$ m is utilized to relate the local near-bottom velocities to local bottom stresses (Kukulka et al., 2011, 2012). The domain size of the simulation is 160 m × 160 m with 160 × 160 horizontal grid points and 16 m with 64 vertical grid points. The ratio of resolved TKE to total TKE generally exceeds 80%, indicating that our resolution successfully resolves the flux and energy-containing eddies in this study.

The Stokes drift vector in Equation 1 is calculated from the observed two-dimensional wave height spectra ϕ_2 (Kenyon, 1969):

$$\mathbf{u}_s(z) = g\iint_{-\infty}^{\infty}\phi_2(\mathbf{k})\frac{\mathbf{k}}{2\pi F}\frac{2kcosh(2k(z+H))}{sinh(2kH)}d\mathbf{k}, \tag{2}$$

where $\mathbf{k}$ is the wave number vector, $k = |\mathbf{k}|$ is the magnitude of wave number vector satisfying the dispersion relationship of surface gravity waves at intermediate depth $F = \sqrt{gk\,tanh(kH)}/2\pi$, and $\phi_2(\mathbf{k})$ is the two-dimensional wave height spectra in wavenumber coordinates.

Five LES experiments under different wind, wave, and wind fetch conditions are designed to compare to the observation, illustrating how complex wind and wave conditions impact LT dynamics. The experiments e1, e2, and e3 are forced by the observed wind and Stokes drift, corresponding to events t1 (misaligned wind and waves), t2 (aligned wind and waves), and t3 (misaligned wind and swell-dominated waves). To further demonstrate the effects of wind–wave misalignments on LT, experiment e4 is conducted with the same forcing as e1 but assuming the Stokes drift is aligned with wind direction. The experiment e5 includes only wind-driven shear turbulence based on the e3 wind condition, designed as a control group. For convenient comparison, the x-direction is chosen toward the wind direction for all LES experiments, and the observed Stokes drift vectors are projected into along-wind and crosswind directions. Each LES experiment spins up for 24 hr, so that turbulent fields reach a stationary state, which is investigated in this study.

3. Results

3.1. Wave Responses to Different Wind Directions

3.1.1. Observational Results

In the coastal ocean, the directions of observed winds and waves are frequently misaligned even with relatively stationary wind conditions (Figure 2). To clearly display the misalignments of wind and waves, the two-dimensional wave height spectra for events t1–t3 are first examined (Figure 3). For oblique offshore winds (t1), the wind and waves are significantly misaligned with the misalignment angle of about 90° (Figure 3a). The high-frequency wind-driven waves barely develop along the wind direction because the offshore fetch is much shorter than alongshore and onshore fetches. A relatively weak southerly swell wave appears in the low-frequency part of the wave height spectrum due to unlimited fetch in that direction. For oblique onshore winds (t2), much longer wind fetch allows wind-driven waves to develop more and align with the wind direction (Figure 3b). Meanwhile, the swell waves direction is similar to t1. For offshore winds (t3), high-frequency wind-driven waves are much less developed due to the short fetch, and low-frequency onshore swell waves dominate the wave height spectrum (Figure 3c). For each event, the Stokes drift is calculated from the two-dimensional wave height spectra by Equation 2. The directions of the surface Stokes drift ($z = 0$ m) are roughly consistent with the directions of the spectral peak so that the wind vectors and surface Stokes drifts are substantially misaligned for t1 and t3. These misalignments greatly affect wave-driven LT, demonstrated in Sections 3.2 and 3.3. The wave height spectra

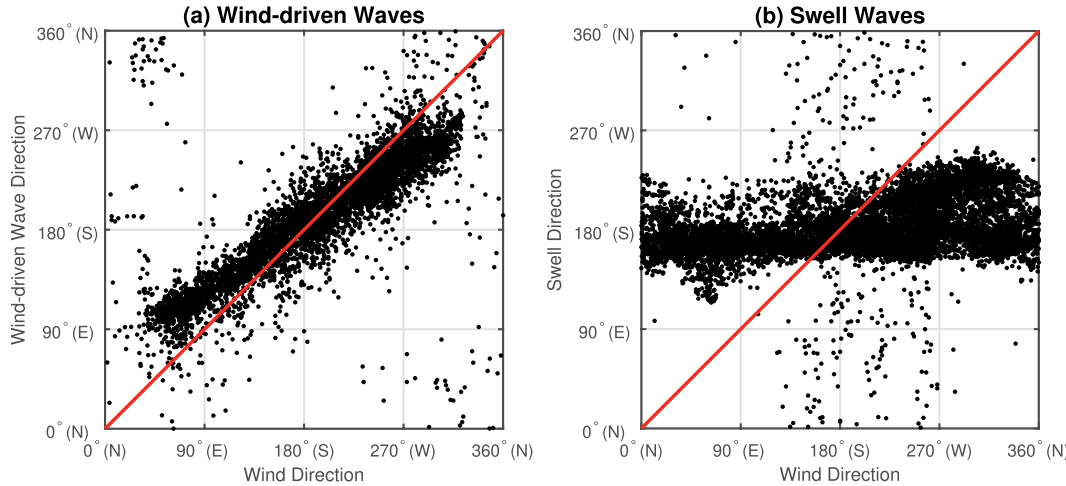

Figure 4. Observed wind directions versus observed directions of (a) wind-driven waves and (b) swell waves. Each dot represents a data point in the time series in Figure 2.

also reveal that low-frequency swell waves, propagating toward land, contain significant energy but dominate the near-surface Stokes drift direction only if higher frequency waves are relatively weak. This is expected as the surface Stokes drift is strongly influenced by the high-frequency part of the wave spectrum.

To further investigate the relationship between wind and wave directions, we also examine directions of wind waves and swell waves, respectively, based on the full CBLAST-low period. The observation reveals that the misalignments of wind and wind-driven waves are significantly related to the wind directions (Figure 4a). For onshore and oblique onshore winds (>90° and <270°), the directions of wind-driven waves and wind are roughly aligned, especially for southerly onshore winds (close to 180°). Such aligned wind and waves are consistent with the wave spectrum of t2 driven by an oblique onshore wind (Figure 3b). For alongshore winds (about 90° and 270°) and oblique offshore winds (<90° or >270°), the wave direction is biased toward 180° (Figure 4a), also because the fetch is longer for directions from 90° to 270°. This bias is due to the misaligned wind and waves, as shown in the wave spectrum of t1 with oblique offshore winds (Figure 3a). For offshore winds (close to 0°/360°), short wind fetch limits wave development so that a significant wind-driven wave spectrum may not always be detected (Figure 4a), consistent with the wave spectrum of t3 driven by an offshore wind (Figure 3c). For swell waves, the northern land boundary only allows persistent southerly swell waves, independent of the wind direction (Figure 4b). Hence, swell waves have a relatively constant direction and can be significantly misaligned with wind and wind-driven waves.

Thus far, the analysis of wave height spectra of the selected events and the statistical comparison between wind and wave directions indicate that the wind–wave misalignments are related to the wind directions, which is also demonstrated by the wave model results.

3.1.2. Wind–Wave Simulation

Considering the fetch-limited conditions for coastal ocean waves, the analysis based on the idealized wave model is insightful to identify the wind fetch influence on the wind and wave misalignments. The simulated wind-driven wave height spectra at three different distances from shore, $d = 3$, 10, and 50 km, are examined for all three experiments NW, SW, and N (Figure 5). Note that a distance of about 3 km south from shore is consistent with the location of the CBLAST-low measurement site. The simulated wave height spectra at $d = 3$ km (Figures 5a–5c) agree well with the observations for the wind–wave portion of the spectrum (Figure 3).

For the NW experiment, offshore wind-driven waves are limited by wind fetch, but the infinite fetch along the shore allows more developed alongshore wind-driven waves (Figures 5a–5c). At $d = 3$ km, wave directions are biased toward shore (Figure 5a), resulting in a substantial misalignment of wind and waves. This is because wind waves are generated within ±90° of the wind direction, including longer southerly and alongshore fetches, at which directions wave components are less fetch limited and more developed. The wind–wave misalignment

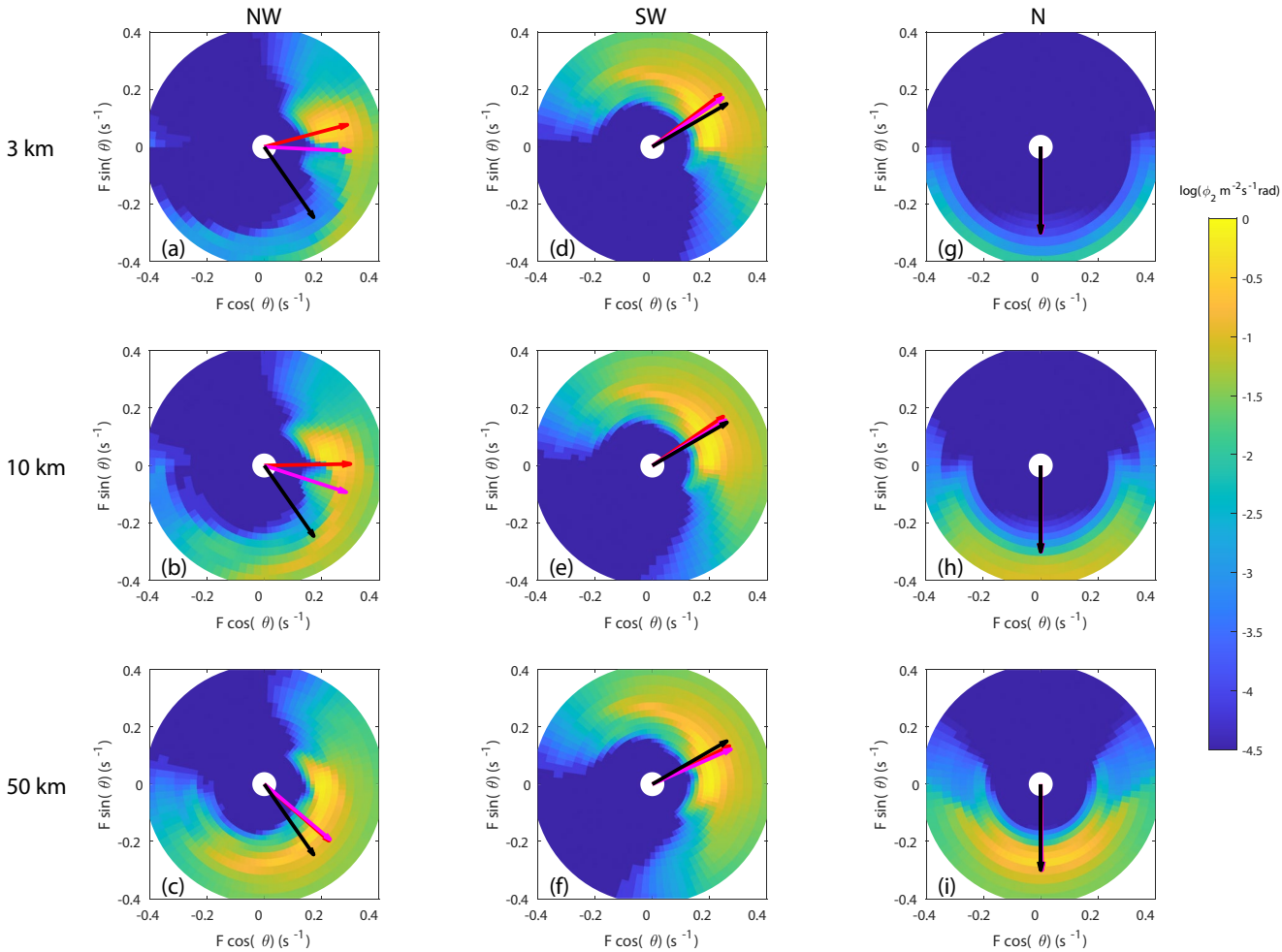

Figure 5. Wave height spectra of wave model results with winds blowing from (left row) 325° (experiment NW), (middle row) 240° (experiment SW), and (right row) 360° (experiment N) for (top panels) 3 km, (center panels) 10 km, and (bottom panels) 50 km south from shore. The arrows are the same as in Figure 3. The wave propagation and arrow direction use Cartesian convention.

gradually decreases to zero as the distance to shore increases, because the increased fetch from shore permits the development of offshore waves (Figures 5b and 5c). The simulated wind–wave misalignment in the NW experiment (Figure 5a) is somewhat smaller than observed (Figure 3a), possibly because the idealized numerical experiments neglect swell waves. Not surprisingly, the observed and simulated surface Stokes drift directions agree better than wave directions as low-frequency swell waves contribute less to the surface Stokes drift and barely affect the direction of surface Stokes drift (Figures 3a and 5a). For the SW experiment, wind-driven waves nearly fully develop for all distances with similar wave height spectra due to the long wind fetch (Figures 5d–5f). For the N experiment, wind-driven waves only weakly develop at 3 km because of the short fetch (Figure 5g), consistent with observations (Figure 3c). Because swell waves are ignored in the wave model, the direction of simulated surface Stokes drift is still the same as the wind direction despite wind waves being weak (Figure 5g), different from the observation (Figure 3c). As the distance to shore increases, the wind-driven part of the wave spectrum develops, and the peak wave frequency decreases (Figures 5h and 5i).

Overall, the simulated wind-driven wave height spectra at $d = 3$ km agree well with the wind-driven wave part of the observed wave spectra for both magnitudes and distributions. By configuring identical settings but different wind directions and fetches, the idealized SWAN model successfully demonstrates that wind fetch plays a key role in the wind–wave misalignments for coastal oceans. The wind-driven waves are smaller for offshore winds and substantially misaligned with the wind direction for oblique offshore winds, consistent with the directional

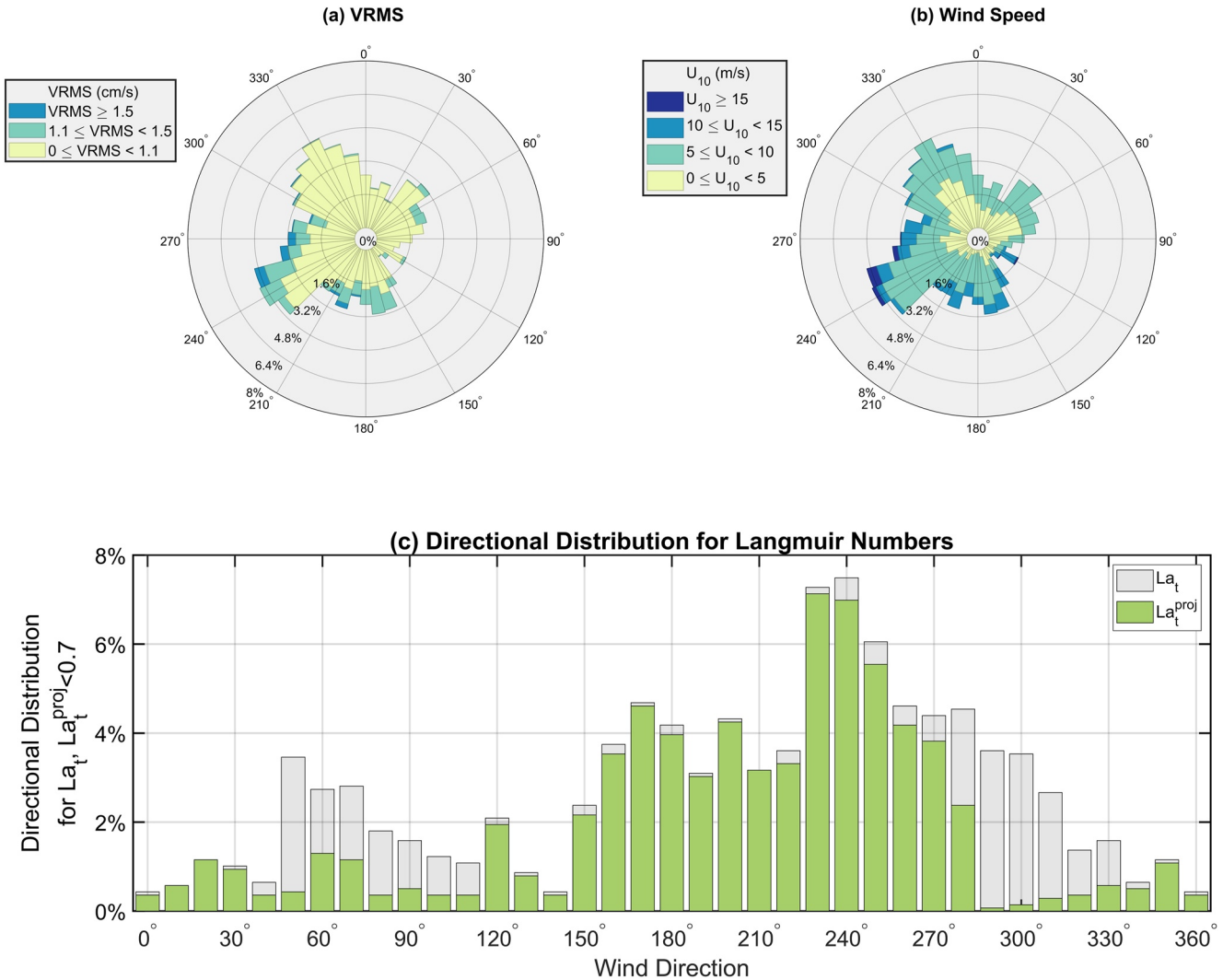

Figure 6. Observed probability distributions of wind direction and (a) VRMS, (b) wind speed, and (c) turbulent Langmuir numbers below 0.7 during the CBLAST-low deployment. The lengths of the color bars represent the proportion of occurrence in the direction range. In panel (c), the lengths of the entire bars represent proportions of occurrence for $La_t < 0.7$, and the green bars represent the parts that $La_t^{proj} < 0.7$. Langmuir turbulence (LT) is expected to be weaker for misaligned conditions when $La_t^{proj} < 0.7$ is significantly less likely than $La_t < 0.7$ (winds blowing from 40° to 110° and 290° to 330°).

distribution of observed wind-driven waves (Figure 4a). These different wave responses to various wind directions in a bounded coastal ocean greatly impact coastal LT activity, discussed subsequently.

3.2. Dependence of Crosswind Velocity Observations on Wind Direction

The wind-directional probability distributions of VRMS and wind speed reveal that the LT strength, indicated by VRMS, is significantly related to the wind direction in a bounded coastal ocean (Figures 6a and 6b). Observed VRMS for winds with northerly components (<90° or >270°) is generally smaller than for winds with southerly wind components (>90° and <270°) and rarely exceeds 1.1 cm/s even for relative strong winds (Figures 6a and 6b). When driven by the winds with northerly components, LT activity is weakest for offshore winds, with VRMS frequently below 0.7 cm/s. For oblique offshore winds, VRMS is larger for strongly oblique offshore winds (close to 90° or 270°) than for weakly oblique ones (close to 0°). This VRMS distribution suggests that coastal LT depends on wind direction and appears more frequently for southerly winds with long fetches during the CBLAST-low experiment.

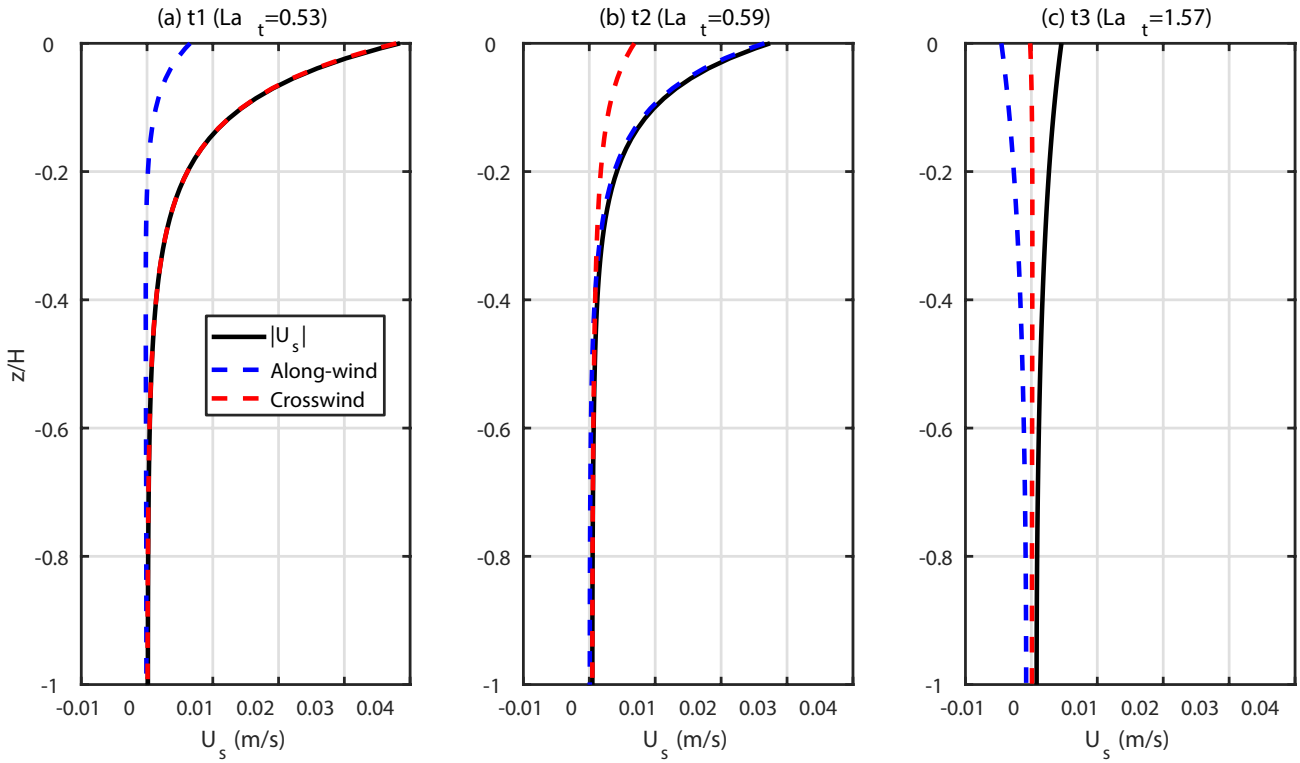

Figure 7. Directional Stokes drift profiles computed from observed wave height spectra for specific events in Figure 2.

To better understand the dependence of LT strength on misalignments of wind and waves, the turbulent Langmuir number $La_t = \sqrt{u_*/|\mathbf{u}_s(0)|}$ (McWilliams et al., 1997) and projected turbulent Langmuir number $La_t^{Proj} = \sqrt{u_*/\left(|\mathbf{u}_s(0)|\cos\theta_{ws}\right)}$ are calculated based on the observation, where $\mathbf{u}_s(0)$ is the surface Stokes drift calculated from observed wave height spectra and θ_{ws} is the misalignment angle of wind and surface Stokes drift directions.

Previous open ocean LT studies indicate that the wind and wave forcings should be projected onto the direction of depth-averaged Lagrangian shear for scaling of LT in misaligned wind–wave conditions (Van Roekel et al., 2012; D. Wang et al., 2019). Note that La_t^{proj} is consistent with the projected Langmuir number from Van Roekel et al. (2012) if the Lagrangian shear is aligned with the wind. This is approximately the case in our study because the wind-driven Eulerian shear often substantially exceeds the Stokes drift shear (Kukulka et al., 2011).

For aligned wind and wave conditions in a coastal ocean, LT is expected to be present for $La_t < 0.7$ with VRMS > 1.1 cm/s (Kukulka et al., 2011; Tejada-Martínez & Grosch, 2007). This is consistent with our observations for wind directions from 120° to 270° when $La_t \approx La_t^{proj}$ (Figure 6c) so that the events with VRMS > 1.1 cm/s frequently occur (Figure 6a). However, for misaligned wind and waves due to the wind fetch limitation (wind directions from 3000° to 60°), La_t^{proj} is significantly larger than La_t (Figure 6c), which coincides with relatively weak LT activity (Figure 6a). Overall, the qualitatively similar distributions of VRMS and La_t^{Proj} support that LT strength generally weakens for misaligned wind and wave conditions.

To demonstrate the influence of misaligned wind and waves, we examine the Stokes drift profile and contrast the LT response to different wind–wave misalignments for t1–t3. The observation at t1 includes relatively large surface Stokes drift with $La_t = 0.53$ and a Stokes drift that is dominated by crosswind components due to fetch limitation in the offshore direction (Figure 7a). Observations at t2 are characterized by $La_t = 0.59$, which is close to La_t for t1, but wind and waves are much more aligned (Figure 7b). Although the wavefield at t3 is dominated by substantial southerly swell, the Stokes drift is much smaller than at t1 and t2 because low-frequency, long-wavelength swell contributes little to the Stokes drift shear compared to more developed wind-driven waves, especially near the ocean surface (Figure 7c).

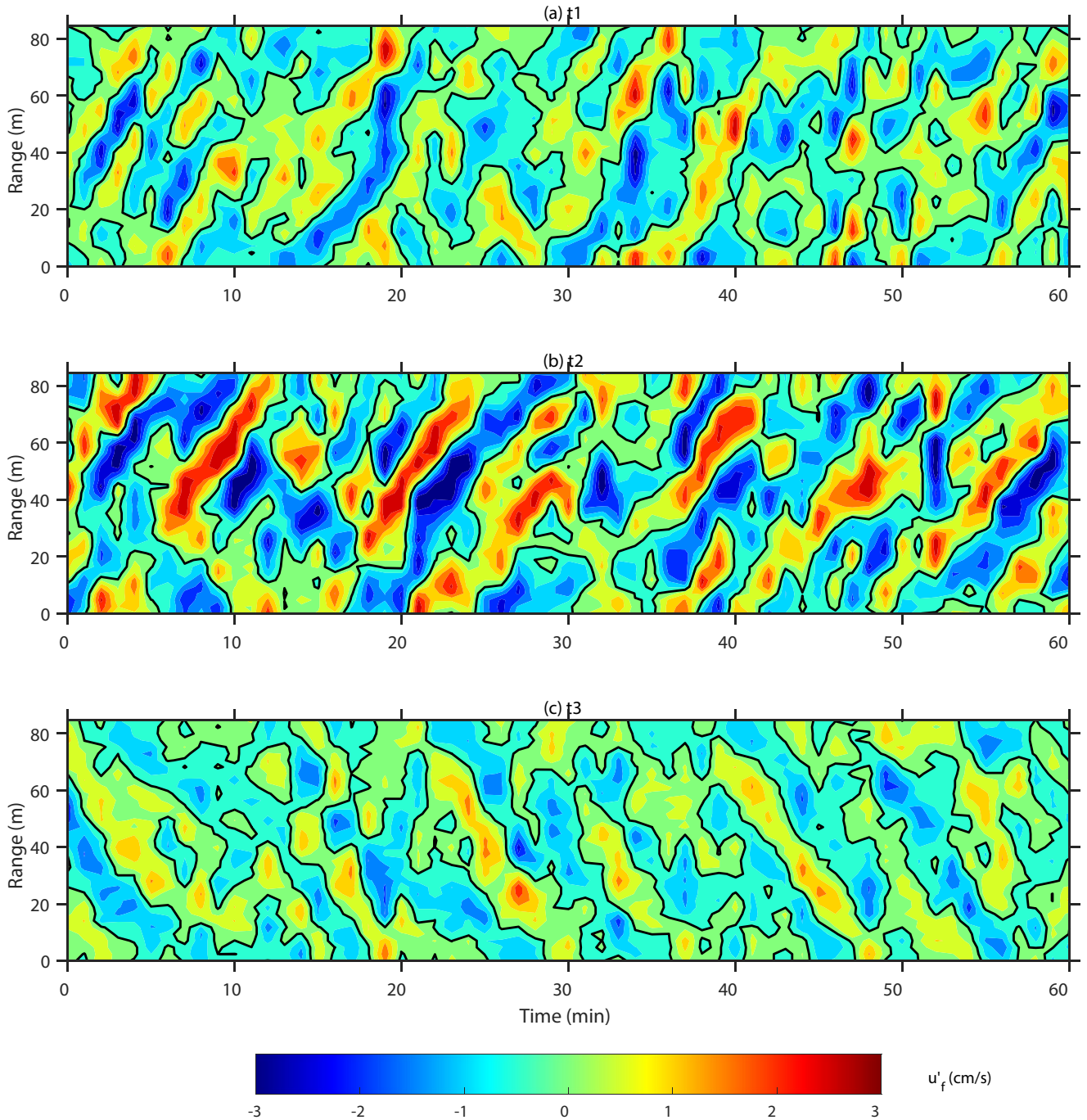

Figure 8. Observed near-surface velocity anomaly u'_f, as function of time and fan-beam range for time close to (a) t1, (b) t2, and (c) t3 (time = 0 min at t1–t3, respectively).

The observed crosswind velocity variations also reveal different LT strengths for the three events (Figure 8). For t2, LT is relatively strong with coherent structures of near-surface convergence and divergence flows driven by wind-aligned waves. The LT strengths for t1 and t3 are much weaker than for t2. For t1, the large wind–wave misalignment due to fetch limitation leads to weak LT even in the presence of a relatively strong Stokes drift (Figure 7a). For t3, the small Stokes drift due to swell-dominated wave fields results in weak LT with less organized near-surface convergence and divergence regions. Thus, the observations indicate that misaligned wind and waves are an important factor for inhibiting coastal LT.

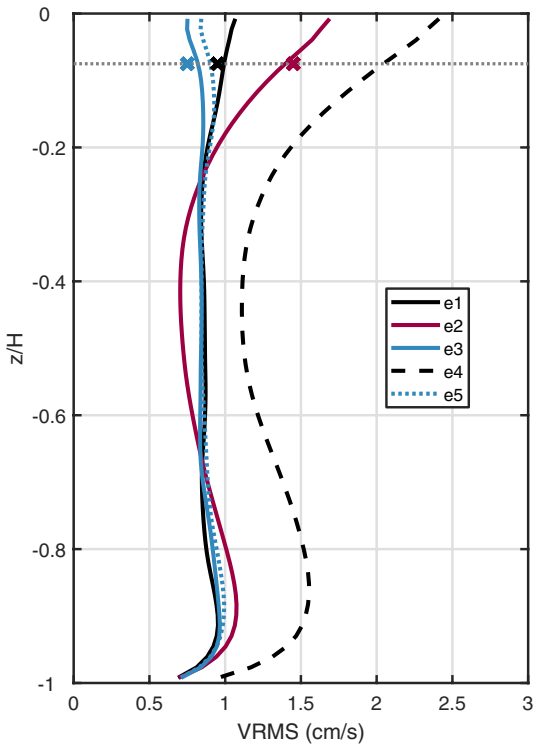

Figure 9. Spatially and temporally averaged profiles of large eddy simulation (LES) simulated VRMS for stationary conditions. e1–e3 are LES experiments with the same forcing as the events in Figure 2. e4 is forced by e1 wind but aligned Stokes drift, and e5 includes only wind-driven shear turbulence based on the e3 wind. Cross signs are the fan-beam VRMS at t1 (black), t2 (red), and t3 (blue). The gray dashed line is $z = 1.2$ m, corresponding to the response to the weighted depth-range of fan-beam instruments.

3.3. Comparison With LES

To confirm that wave development and wind–wave misalignment affect LT strength, we also perform idealized LES for events t1–t3. In order to directly compare the LES results with fan-beam ADCP observation, we first average LES results to adhere to the observations (1 min in time and 3 m × 5 m in space) and then apply the same postprocess as the fan-beam observations on the averaged LES data. Here, we denote the LES processed crosswind velocity variations as simulated u'_f and the associated root-mean-square as simulated VRMS. Note that although TKE is a common indicator for turbulence strength, the near-surface crosswind velocity variation is specifically indicative of LT activity due to relatively strong coherent and converging crosswind flows. The simulated VRMS is 1, 1.4, and 0.75 cm/s for e1, e2, and e3, respectively, at the depth $z = 1.2$ m, corresponding to the typical depth-range response of the fan-beam instruments. The simulated VRMS quantitatively agrees well to the observed VRMS (Figure 9), further indicating that wind–wave misalignment strongly impacts coastal LT.

Because of the presence of strong LT, the simulated VRMS of e2 exceeds that of e1, which is close to the ST case (e5), for $z/H > -0.2$ (Figure 9). However, if the Stokes drift and wind stress from e1 are aligned (e4), the simulated VRMS is elevated and becomes greater than that of e2 due to the stronger wind and wave forcing. This distinct difference between simulated VRMS for e1 and e4 demonstrates that wind–wave misalignments in e1 substantially decrease LT strength. The close agreement between simulated VRMS for the swell case e3 and for the ST case e5 indicates that swell waves have only a minor influence on the LT development for the offshore winds during the CBLAST-low experiment.

Consistent with the profiles of simulated VRMS, the simulated crosswind velocity variations u'_f present more organized structures with coherent near-surface convergence and divergence regions for experiments with relatively aligned wind and waves (e2 and e4) than other experiments (Figure 10). The LT width (distance between convergence regions) is about 50 m, $>2H$, and Langmuir cells likely extend throughout the entire water column (Gargett et al., 2004). The experiment with significant wind–wave misalignment (e1) and the experiment with dominant swell (e3) display relatively disorganized convergence and divergence regions, similar to the ST case (e5), indicating relatively weak LT. Moreover, the simulated u'_f and crosswind length scales for e1–e3 also quantitatively agrees well with the observed fan-beam u'_f (Figure 8).

Although the convergence and divergence regions are weaker and more irregular for the ST case, they still display weaker Couette cells (Tejada-Martínez & Grosch, 2007). For the e1 experiment, the crosswind Stokes drift induces an anti-Stokes Eulerian current, leading to a minor Lagrangian velocity shear in the crosswind direction (not shown here). The appearance of the anti-Stokes Eulerian current is consistent with the misaligned wind-wave studies for the open ocean (Pearson, 2018), which reveal the complex relationship between Reynolds stress and velocity shear (D. Wang & Kukulka, 2021). The agreements of LES and fan-beam observations have demonstrated that the wind fetch and direction, as well as wind–wave misalignment, significantly influence the LT strength in a bounded coastal ocean.

4. Conclusion

This study investigates how wind fetch and wind direction affect LT at a coastal site south of the island Martha's Vineyard (MA, USA). Based on the analysis of observations and numerical simulations, we provide evidence of reduced LT due to misaligned wind and waves. Observations from the CBLAST-low experiment include meteorological forcing data, wave measurements, and surface velocity from special-purpose instrumentation. The

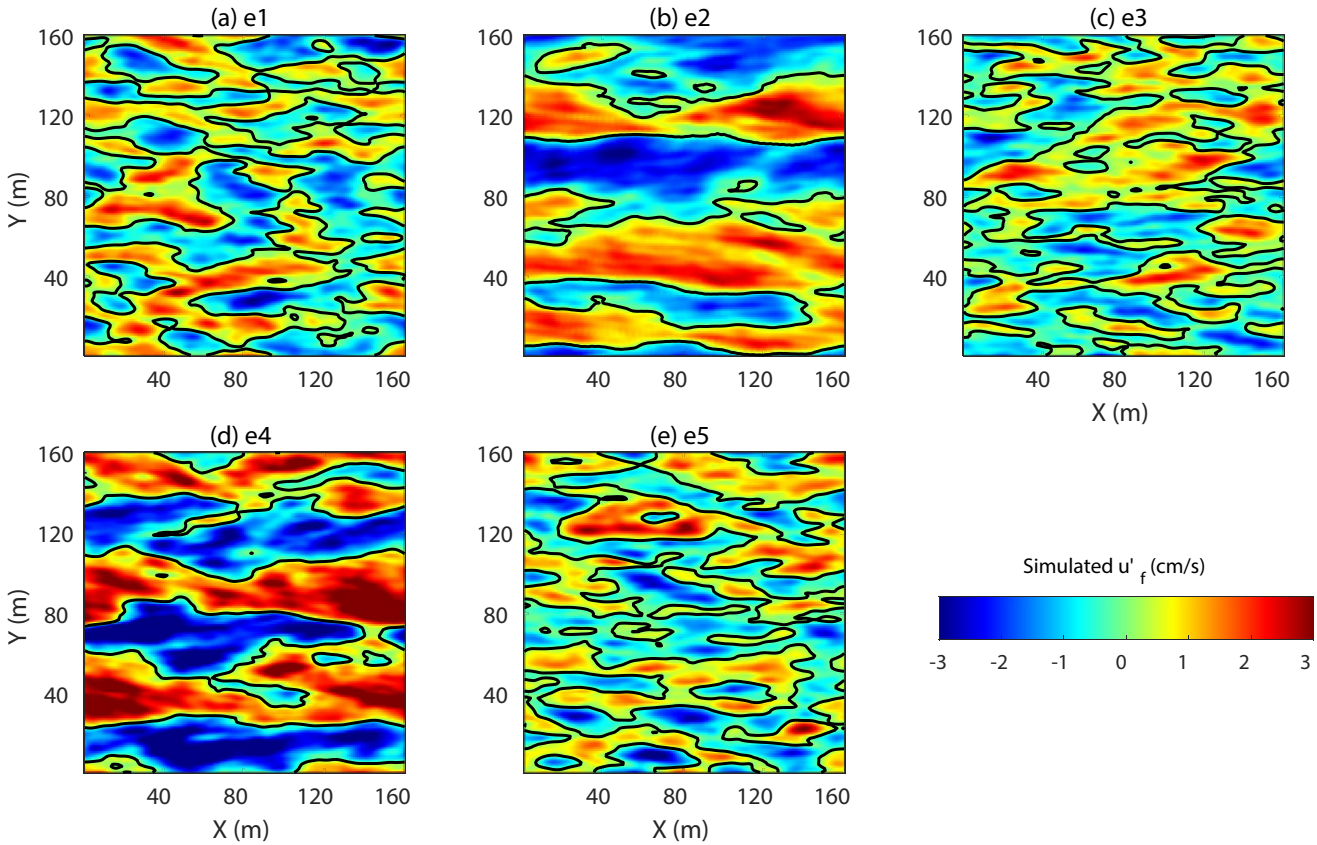

Figure 10. Horizontal cross sections of the processed crosswind velocity variation u'_f at $z = 1.2$ m under stationary conditions for five LES experiments described in Figure 9.

observed crosswind surface velocity is enhanced in the presence of LT due to near-surface coherent convergent flows. The observed velocity fields are directly compared to results from turbulence-resolving LES. The root-mean-square of the observed crosswind velocity anomaly (VRMS) is calculated to quantify the LT strength.

At our study site, wind direction controls wind fetch, an important factor in forming wave development and wind–wave misalignment. For northerly offshore winds, limited wind fetch results in limited wave development, while onshore winds from the south are associated with a practically infinite fetch with substantial wave development. For oblique offshore winds, the less limited wind fetch along the shore allows more developed wind-driven waves, resulting in large misalignments between wind and waves. The results from the wave model, validated by the observed wave height spectra, confirm the controlling influence of fetch on misaligned wind and waves because the misalignments decrease as wind fetch increases. These wind–wave misalignments are characteristic of coastal sites and greatly affect LT activity.

The observed VRMS is significantly correlated with the wind direction. Strong LT is only present for sufficiently developed waves, excluding the formation of LT for fetch-limited northerly offshore winds. For oblique offshore winds, the VRMS for weakly oblique winds is generally smaller than for strongly oblique ones because of more misaligned wind and waves. At the study site, energetic and persistent southerly swell waves are too long to influence LT activity substantially during the observation period because of their relatively weak near-surface Stokes drift shear.

Forced by the observed wind and waves, the VRMS of turbulence-resolving LES agrees well with the observed VRMS. This agreement contributes to validating the LES approach to coastal LT for complex wind and wave conditions. Additionally, both observation and LES results reveal less organized convergence and divergence patterns for misaligned wind and waves and more organized patterns for aligned wind and waves, confirming that misaligned wind and waves weaken LT activity. Thus, our study demonstrates that wind fetch and direction

strongly influence coastal LT by limiting wave development and controlling wind–wave misalignment, which needs to be taken into account for understanding wave-driven coastal transport processes.

Notably, this study demonstrates that misaligned wind and waves weaken coastal LT based on unique paired observation and idealized simulation. However, the forcing condition is complex for the coastal ocean. A more comprehensive study may also need to consider the effects of variable wind stress, background currents, and diurnal heating to better understand coastal LT dynamics.

Data Availability Statement

The CBLAST-low data can be accessed through the Woods Hole Oceanographic Institution website (https://mvco.whoi.edu/cblast-low/). The numerical results used in this study are simulated by National Center for Atmospheric Research Large Eddy Simulation model initially established by Moeng (1984) and operated with the numeric scheme of Sullivan et al. (1996).

Acknowledgments
We acknowledge the support of National Science Foundation grant OCE-1634578 for funding this work. The Office of Naval Research funded the CBLAST-low experiment. This research was supported in part through the use of Information Technologies (IT) resources at the University of Delaware, specifically the high-performance computing resources.

References

Booij, N., Holthuijsen, L., & Ris, R. (1997). The "swan" wave model for shallow water. *Coastal Engineering*, *1996*, 668–676. https://doi.org/10.1061/9780784402429.053

Churchill, J. H., Plueddemann, A. J., & Faluotico, S. M. (2006). *Extracting wind sea and swell from directional wave spectra derived from a bottom-mounted ADCP (Tech. Rep.)*. Woods Hole, MA: Woods Hole Oceanographic Institution.

Craik, A. D., & Leibovich, S. (1976). A rational model for Langmuir circulations. *Journal of Fluid Mechanics*, *73*(3), 401–426. https://doi.org/10.1017/s0022112076001420

D'Asaro, E. A. (2014). Turbulence in the upper-ocean mixed layer. *Annual Review of Marine Science*, *6*, 101–115. https://doi.org/10.1146/annurev-marine-010213-135138

D'Asaro, E. A., Thomson, J., Shcherbina, A., Harcourt, R., Cronin, M., Hemer, M., & Fox-Kemper, B. (2014). Quantifying upper ocean turbulence driven by surface waves. *Geophysical Research Letters*, *41*, 102–107. https://doi.org/10.1002/2013GL058193

Deng, B.-Q., Yang, Z., Xuan, A., & Shen, L. (2019). Influence of Langmuir circulations on turbulence in the bottom boundary layer of shallow water. *Journal of Fluid Mechanics*, *861*, 275–308. https://doi.org/10.1017/jfm.2018.883

Edson, J., Crawford, T., Crescenti, J., Farrar, T., Frew, N., Gerbi, G., et al. (2007). The coupled boundary layers and air–sea transfer experiment in low winds. *Bulletin of the American Meteorological Society*, *88*(3), 341–356. https://doi.org/10.1175/bams-88-3-341

Farmer, D., & Li, M. (1995). Patterns of bubble clouds organized by Langmuir circulation. *Journal of Physical Oceanography*, *25*(6), 1426–1440. https://doi.org/10.1175/1520-0485(1995)025<1426:POBCOB>2.0.CO;2

Fisher, A. W., Sanford, L. P., Scully, M. E., & Suttles, S. E. (2017). Surface wave effects on the translation of wind stress across the air–sea interface in a fetch-limited, coastal embayment. *Journal of Physical Oceanography*, *47*(8), 1921–1939. https://doi.org/10.1175/jpo-d-16-0146.1

Gargett, A. E., & Wells, J. R. (2007). Langmuir turbulence in shallow water. Part 1. Observations. *Journal of Fluid Mechanics*, *576*, 27–61. https://doi.org/10.1017/s0022112006004575

Gargett, A. E., Wells, J. R., Tejada-Martínez, A. E., & Grosch, C. (2004). Langmuir supercells: A mechanism for sediment resuspension and transport in shallow seas. *Science*, *306*(5703), 1925–1928. https://doi.org/10.1126/science.1100849

Gerbi, G. P., Trowbridge, J. H., Terray, E. A., Plueddemann, A. J., & Kukulka, T. (2009). Observations of turbulence in the ocean surface boundary layer: Energetics and transport. *Journal of Physical Oceanography*, *39*(5), 1077–1096. https://doi.org/10.1175/2008jpo4044.1

Grant, A. L., & Belcher, S. E. (2009). Characteristics of Langmuir turbulence in the ocean mixed layer. *Journal of Physical Oceanography*, *39*(8), 1871–1887. https://doi.org/10.1175/2009jpo4119.1

Hanson, J. L., & Phillips, O. M. (2001). Automated analysis of ocean surface directional wave spectra. *Journal of Atmospheric and Oceanic Technology*, *18*(2), 277–293. https://doi.org/10.1175/1520-0426(2001)018<0277:AAOOSD>2.0.CO;2

Harcourt, R. R., & D'Asaro, E. A. (2008). Large-eddy simulation of Langmuir turbulence in pure wind seas. *Journal of Physical Oceanography*, *38*(7), 1542–1562. https://doi.org/10.1175/2007jpo3842.1

Kenyon, K. E. (1969). Stokes drift for random gravity waves. *Journal of Geophysical Research*, *74*(28), 6991–6994. https://doi.org/10.1029/JC074i028p06991

Kukulka, T., & Harcourt, R. R. (2017). Influence of Stokes drift decay scale on Langmuir turbulence. *Journal of Physical Oceanography*, *47*(7), 1637–1656. https://doi.org/10.1175/jpo-d-16-0244.1

Kukulka, T., Jenkins, R. L., III, Kirby, J. T., Shi, F., & Scarborough, R. W. (2017). Surface wave dynamics in Delaware bay and its adjacent coastal shelf. *Journal of Geophysical Research: Oceans*, *122*, 8683–8706. https://doi.org/10.1002/2017JC013370

Kukulka, T., Plueddemann, A., & Sullivan, P. (2012). Nonlocal transport due to Langmuir circulation in a coastal ocean. *Journal of Geophysical Research*, *117*, C12007. https://doi.org/10.1029/2012JC008340

Kukulka, T., Plueddemann, A. J., Trowbridge, J. H., & Sullivan, P. P. (2009). Significance of Langmuir circulation in upper ocean mixing: Comparison of observations and simulations. *Geophysical Research Letters*, *36*, L10603. https://doi.org/10.1029/2009GL037620

Kukulka, T., Plueddemann, A. J., Trowbridge, J. H., & Sullivan, P. P. (2011). The influence of crosswind tidal currents on Langmuir circulation in a shallow ocean. *Journal of Geophysical Research*, *116*, C08005. https://doi.org/10.1029/2011JC006971

Lentz, S. J. (1995). Sensitivity of the inner-shelf circulation to the form of the eddy viscosity profile. *Journal of Physical Oceanography*, *25*(1), 19–28. https://doi.org/10.1175/1520-0485(1995)025<0019:SOTISC>2.0.CO;2

Li, S., Li, M., Gerbi, G. P., & Song, J.-B. (2013). Roles of breaking waves and Langmuir circulation in the surface boundary layer of a coastal ocean. *Journal of Geophysical Research: Oceans*, *118*, 5173–5187. https://doi.org/10.1002/jgrc.20387

McWilliams, J. C., Sullivan, P. P., & Moeng, C.-H. (1997). Langmuir turbulence in the ocean. *Journal of Fluid Mechanics*, *334*, 1–30. https://doi.org/10.1017/s0022112096004375

Moeng, C.-H. (1984). A large-eddy-simulation model for the study of planetary boundary-layer turbulence. *Journal of the Atmospheric Sciences*, *41*(13), 2052–2062. https://doi.org/10.1175/1520-0469(1984)041<2052:ALESMF>2.0.CO;2

Pearson, B. C. (2018). Turbulence-induced anti-Stokes flow and the resulting limitations of large-eddy simulation. *Journal of Physical Oceanography*, *48*(1), 117–122. https://doi.org/10.1175/jpo-d-17-0208.1

Pearson, B. C., Grant, A. L., & Polton, J. A. (2019). Pressure–strain terms in Langmuir turbulence. *Journal of Fluid Mechanics*, *880*, 5–31. https://doi.org/10.1017/jfm.2019.701

Plueddemann, A., Terray, E., & Merewether, R. (2001). Design and performance of a self-contained fan-beam ADCP. *IEEE Journal of Oceanic Engineering*, *26*(2), 252–258. https://doi.org/10.1109/48.922791

Plueddemann, A. J., Smith, J. A., Farmer, D. M., Weller, R. A., Crawford, W. R., Pinkel, R., et al. (1996). Structure and variability of Langmuir circulation during the surface waves processes program. *Journal of Geophysical Research*, *101*(C2), 3525–3543. https://doi.org/10.1029/95JC03282

Shrestha, K., Anderson, W., Tejada-Martínez, A. E., & Kuehl, J. (2019). Orientation of coastal-zone Langmuir cells forced by wind, wave and mean current at variable obliquity. *Journal of Fluid Mechanics*, *879*, 716–743. https://doi.org/10.1017/jfm.2019.683

Skyllingstad, E. D., & Denbo, D. W. (1995). An ocean large-eddy simulation of Langmuir circulations and convection in the surface mixed layer. *Journal of Geophysical Research*, *100*(C5), 8501–8522. https://doi.org/10.1029/94JC03202

Smith, J. A. (1989). Doppler sonar and surface waves: Range and resolution. *Journal of Atmospheric and Oceanic Technology*, *6*(4), 680–696. https://doi.org/10.1175/1520-0426(1989)006<0680:DSASWR>2.0.CO;2

Smith, J. A. (1992). Observed growth of Langmuir circulation. *Journal of Geophysical Research*, *97*(C4), 5651–5664. https://doi.org/10.1029/91JC03118

Sullivan, P. P., & McWilliams, J. C. (2010). Dynamics of winds and currents coupled to surface waves. *Annual Review of Fluid Mechanics*, *42*, 19–42. https://doi.org/10.1146/annurev-fluid-121108-145541

Sullivan, P. P., McWilliams, J. C., & Moeng, C.-H. (1994). A subgrid-scale model for large-eddy simulation of planetary boundary-layer flows. *Boundary-Layer Meteorology*, *71*(3), 247–276. https://doi.org/10.1007/bf00713741

Sullivan, P. P., McWilliams, J. C., & Moeng, C.-H. (1996). A grid nesting method for large-eddy simulation of planetary boundary-layer flows. *Boundary-Layer Meteorology*, *80*(1), 167–202. https://doi.org/10.1007/bf00119016

Tejada-Martínez, A. E., & Grosch, C. E. (2007). Langmuir turbulence in shallow water. Part 2. Large-eddy simulation. *Journal of Fluid Mechanics*, *576*, 63–108. https://doi.org/10.1017/s0022112006004587

Tejada-Martínez, A. E., Grosch, C. E., Sinha, N., Akan, C., & Martinat, G. (2012). Disruption of the bottom log layer in large-eddy simulations of full-depth Langmuir circulation. *Journal of Fluid Mechanics*, *699*, 79–93. https://doi.org/10.1017/jfm.2012.84

Thorpe, S. (2004). Langmuir circulation. *Annual Review of Fluid Mechanics*, *36*, 55–79. https://doi.org/10.1146/annurev.fluid.36.052203.071431

Van Den Bremer, T., & Breivik, Ø. (2018). Stokes drift. *Philosophical Transactions of the Royal Society A: Mathematical, Physical & Engineering Sciences*, *376*(2111), 20170104. https://doi.org/10.1098/rsta.2017.0104

Van Roekel, L., Fox-Kemper, B., Sullivan, P., Hamlington, P., & Haney, S. (2012). The form and orientation of Langmuir cells for misaligned winds and waves. *Journal of Geophysical Research*, *117*, C05001. https://doi.org/10.1029/2011JC007516

Wang, D., & Kukulka, T. (2021). Wind- and wave-driven Reynolds stress and velocity shear in the upper ocean for idealized misaligned wind–wave conditions. *Journal of Physical Oceanography*, *51*(2), 633–644. https://doi.org/10.1175/jpo-d-20-0157.1

Wang, D., Kukulka, T., Reichl, B. G., Hara, T., & Ginis, I. (2019). Wind–wave misalignment effects on Langmuir turbulence in tropical cyclone conditions. *Journal of Physical Oceanography*, *49*(12), 3109–3126. https://doi.org/10.1175/jpo-d-19-0093.1

Wang, X., & Kukulka, T. (2021). Ocean surface boundary layer response to abruptly turning winds. *Journal of Physical Oceanography*, *51*(6), 1779–1794. https://doi.org/10.1175/jpo-d-20-0198.1

Weller, R. A., Dean, J. P., Price, J. F., Francis, E. A., Marra, J., & Boardman, D. C. (1985). Three-dimensional flow in the upper ocean. *Science*, *227*(4694), 1552–1556. https://doi.org/10.1126/science.227.4694.1552

Zedel, L., & Farmer, D. (1991). Organized structures in subsurface bubble clouds: Langmuir circulation in the open ocean. *Journal of Geophysical Research*, *96*(C5), 8889–8900. https://doi.org/10.1029/91JC00189